Magnetic resonance imaging of spin-wave transport and interference in a magnetic insulator

Bertelli, Iacopo; Carmiggelt, Joris J.; Yu, Tao; Simon, Brecht G.; Pothoven, Coosje C.; Bauer, Gerrit E.W.; Blanter, Yaroslav M.; Aarts, Jan; van der Sar, Toeno

DOI
10.1126/sciadv.abd3556

Publication date
2020

Document Version
Final published version

Published in
Science Advances

Citation (APA)
Bertelli, I., Carmiggelt, J. J., Yu, T., Simon, B. G., Pothoven, C. C., Bauer, G. E. W., Blanter, Y. M., Aarts, J., & van der Sar, T. (2020). Magnetic resonance imaging of spin-wave transport and interference in a magnetic insulator. *Science Advances*, *6*(46), Article eabd3556. https://doi.org/10.1126/sciadv.abd3556

APPLIED SCIENCES AND ENGINEERING

Magnetic resonance imaging of spin-wave transport and interference in a magnetic insulator

Iacopo Bertelli[1,2], Joris J. Carmiggelt[1], Tao Yu[1,3], Brecht G. Simon[1], Coosje C. Pothoven[1], Gerrit E. W. Bauer[1,4], Yaroslav M. Blanter[1], Jan Aarts[2], Toeno van der Sar[1]*

Spin waves—the elementary excitations of magnetic materials—are prime candidate signal carriers for low-dissipation information processing. Being able to image coherent spin-wave transport is crucial for developing interference-based spin-wave devices. We introduce magnetic resonance imaging of the microwave magnetic stray fields that are generated by spin waves as a new approach for imaging coherent spin-wave transport. We realize this approach using a dense layer of electronic sensor spins in a diamond chip, which combines the ability to detect small magnetic fields with a sensitivity to their polarization. Focusing on a thin-film magnetic insulator, we quantify spin-wave amplitudes, visualize spin-wave dispersion and interference, and demonstrate time-domain measurements of spin-wave packets. We theoretically explain the observed anisotropic spin-wave patterns in terms of chiral spin-wave excitation and stray-field coupling to the sensor spins. Our results pave the way for probing spin waves in atomically thin magnets, even when embedded between opaque materials.

INTRODUCTION

Over the last few decades, the desire to understand and control spin transport, and to use it in information technology, has invigorated the field of spintronics. A central goal of the field is to provide information processing based on the spin of the electron instead of its charge and thereby avoid the heating associated with charge currents. As heating is currently the main obstacle for increasing computational speed, spin-based information processing may provide the next transformative change in information technology.

Promising signal carriers for low-dissipation information transport are spin waves (*1*, *2*)—the collective spin excitations of magnetic materials. Spin waves exist even in electrically insulating magnets, where they are able to propagate inherently free of the dissipative motion of charge. They can have nanometer wavelengths and gigahertz frequencies well suited for chip-scale device technologies and interference-based spin-wave logic circuits (*2*). Consequently, a growing research field focuses on spin-wave devices such as interconnects, interferometers, transistors, amplifiers, and spin-torque oscillators (*3*–*7*).

Being able to image coherent spin waves in thin-film magnets is crucial for developing spin-wave device technology. Leading techniques for imaging coherent spin waves, such as transmission x-ray microscopy (*8*, *9*), Brillouin light scattering (*10*), and Kerr microscopy (*11*), rely on a spin-dependent optical response of a magnetic material. Here, we introduce a new approach: phase-sensitive magnetic resonance imaging of the microwave magnetic stray fields generated by coherent spin waves. We realize this approach using a layer of electronic sensor spins in a diamond chip as imaging platform (Fig. 1A). These spins enable quantitative measurements of microwave magnetic fields including their polarization, making the approach well suited for spin-wave imaging in magnetic thin films. Focusing on a ~200-nm-thick magnetic insulator, we quantify spin-wave amplitudes, visualize the spin-wave dispersion, and demonstrate time-domain measurements of spin-wave packets. We observe unidirectional emission of spin waves that autofocus, interfere, and produce chiral magnetic stray fields with a handedness that matches that of the natural precession of the sensor spins. We present a theoretical analysis of the chiral spin-wave excitation and stray-field coupling to the sensor spins and show that it accurately describes the observed spatial spin-wave maps.

We detect the magnetic fields generated by spin waves using electron spins associated with nitrogen-vacancy (NV) lattice defects in diamond (*12*). These spins can be initialized and read out optically and manipulated with high fidelity by microwaves. Over the last decade, NV magnetometry has emerged as a powerful platform for probing static and dynamic magnetic phenomena in condensed matter systems (*13*). Key is an NV-sample distance tunable between 10 and 1000 nm that is well matched with the length scales of spin textures such as magnetic domain walls, cycloids, vortices, and skyrmions (*14*–*16*) as well as those of dynamic phenomena such as spin waves (*17*–*21*). Recent experiments demonstrated that NV magnetometry has the sensitivity required for imaging the static magnetization of monolayer van der Waals magnets (*22*). Here, we develop NV-based magnetic resonance imaging into a platform for studying coherent spin waves via the gigahertz magnetic fields that they generate.

RESULTS

Our imaging platform consists of a diamond chip hosting a dense layer of shallowly implanted NV spins. We position this chip onto a thin film of yttrium iron garnet (YIG)—a ferrimagnetic insulator with record-high magnetic quality (Fig. 1, A and B) (*23*). The typical distance between the diamond and the magnetic film is ~1 μm (Supplementary Materials). We excite spin waves using microwave striplines microfabricated onto the YIG. When the spin-wave frequency matches an NV electron spin resonance (ESR) frequency, the oscillating magnetic stray field B_{SW} drives NV spin transitions (*17*, *19*) that we detect through the NV's spin-dependent photoluminescence (Materials and Methods). By tuning the external static

[1]Department of Quantum Nanoscience, Kavli Institute of Nanoscience, Delft University of Technology, Lorentzweg 1, 2628 CJ Delft, Netherlands. [2]Huygens-Kamerlingh Onnes Laboratorium, Leiden University, Niels Bohrweg 2, 2300 RA Leiden, Netherlands. [3]Max Planck Institute for the Structure and Dynamics of Matter, Luruper Chaussee 149, 22761 Hamburg, Germany. [4]Institute for Materials Research and WPI-AIMR and CSRN, Tohoku University, Sendai 980-8577, Japan.
*Corresponding author. Email: t.vandersar@tudelft.nl

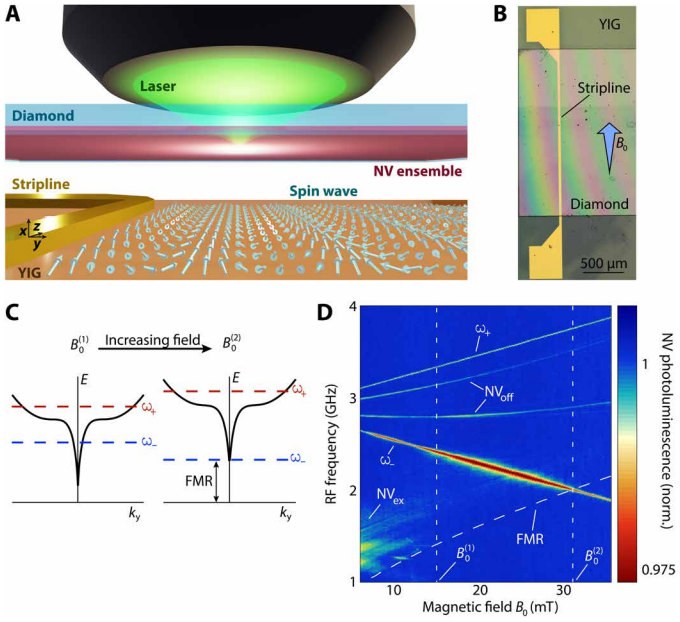

Fig. 1. Imaging spin waves using NV spins in diamond. (**A**) A diamond hosting a layer of NV spins implanted at 20 nm below its surface is placed onto a film of YIG (thickness of 245 nm) grown on gadolinium gallium garnet (GGG). The NVs detect the magnetic fields of stripline-excited spin waves. (**B**) NV-containing diamond (thickness of ~40 μm) on YIG with gold stripline. B_0 is applied along the stripline at $\phi = 35°$ relative to the sample plane, aligning it with one of the four possible NV orientations. (**C**) The NV ESR frequencies $\omega_\pm$ are swept over the Damon-Eshbach spin-wave dispersion (black line) by tuning B_0. For any $B_0^{(1)} < B_0^{(2)}$, ω_- is resonant with spin waves of finite wavelength. At $B_0 = B_0^{(2)}$, ω_- is resonant with the ferromagnetic resonance (FMR). (**D**) Normalized NV photoluminescence versus B_0 and microwave drive frequency, measured at ~5 μm from a 2.5-μm-wide stripline. Indicated are the electronic ground-state ESR transitions $\omega_\pm$ (NV_{off}) of the NVs aligned (not aligned) with B_0. An electronic excited-state ESR transition (NV_{ex}) is visible because of the continuous optical and microwave excitation and identified through its location at $\sim\omega_+/2$ (*12*). The FMR is calculated from the independently determined saturation magnetization (Supplementary Materials).

magnetic field B_0, we sweep the NV ESR frequencies through the spin-wave band, thereby probing spin waves with different wavelength (Fig. 1C).

We start by characterizing the NV photoluminescence as a function of B_0 and the frequency ω_{MW} of a microwave drive current sent through the stripline, at a distance of ~5 μm from the stripline edge (Fig. 1D). This microwave current not only generates an oscillating magnetic field that drives ESR transitions of the NV spins directly but also excites spin waves in the YIG film that can drive NV ESR transitions via their magnetic stray field (Fig. 1A). The dips in the observed NV photoluminescence correspond to the ESR frequencies of the NV spins in the diamond (Fig. 1D; Materials and Methods). We observe an enhanced contrast for the ω_- transition when $B < B_0^{(2)}$. In this region, the excited spin waves efficiently drive the ω_- ESR transition.

We image the spin waves excited by the stripline in the YIG film by characterizing the contrast of the ω_- ESR transition as a function of the distance to the stripline (Fig. 2A). We do so by tuning the magnetic field such that the ω_- frequency is 2.17 GHz, i.e., 160 MHz above the bottom of the spin-wave band, thereby exciting spin waves in the film. To gain the phase sensitivity required for detecting the individual wavefronts of these propagating spin waves, we let their stray field interfere with an additional, externally applied microwave magnetic field B_{REF} that is spatially homogeneous and has the same frequency (Materials and Methods). As formulated mathematically below, this interference leads to a spatial standing-wave pattern in the total magnetic field that drives the NV ESR transition with a spatial periodicity equal to the spin-wave wavelength. We can thus rapidly visualize the spin waves by measuring the ratio between the NV photoluminescence with and without applied microwaves (Fig. 2A).

Quantifying the amplitude of a spin wave is a challenging task for any technique because the coupling between spin wave and probe is often not well known. With NV magnetometry, however, we accurately measure the microwave magnetic field generated by a spin wave as described by Maxwell's equations. We can therefore determine the amplitude of a spin wave of known direction and ellipticity with high confidence by solving a well-defined inverse problem.

To illustrate the concept, we formulate the magnetic stray field of a spin wave traveling perpendicularly to the static magnetization (such as the one in Fig. 2B) in the reference frame depicted in Fig. 1A with transverse magnetization

$$\mathbf{m}_\perp(y) = m_\perp^0 \mathrm{Re}\{e^{i(k_y y-\omega t)}(\hat{\mathbf{y}} - i\eta\hat{\mathbf{x}})\} \quad (1)$$

where k_y, ω, and η are the wave number, angular frequency, and ellipticity of the spin wave, respectively; t is the time; and hats denote unit vectors. This spin wave produces a magnetic stray field above the film that rotates in the xy plane [see the Supplementary Materials and (*24*)]

$$\mathbf{B}_{SW}(y) = -B_{SW}^0 \mathrm{Re}\{e^{i(k_y y-\omega t)}(\hat{\mathbf{y}} + i\mathrm{sgn}(k_y)\hat{\mathbf{x}})\} \quad (2)$$

where $B_{SW}^0 = \mu_0 m_\perp^0(1 + \mathrm{sgn}(k_y)\eta)\,|\mathbf{k}|\,d\,e^{-|k_y|x_0}/2$, x_0 is the NV-YIG distance, and d is the thickness of the YIG film.

The handedness of $\mathbf{B}_{SW}$ is opposite to that of $\mathbf{m}_\perp$ for a spin wave traveling to the right (i.e., with $k_y > 0$; as in Fig. 2B), which drives the ω_- (rather than the ω_+) NV spin transition (Supplementary Materials). Moreover, the amplitude B_{SW}^0 depends on the propagation direction and degree of ellipticity η of the spin wave: Those traveling to the right (left) generate a stronger field above (below) the magnetic film. Therefore, only the ω_- transition of NV centers to the right of the stripline in Fig. 2B is excited (Supplementary Materials). The resulting NV spin rotation rate (Rabi frequency) ω_{Rabi} is determined by the interference between the spin-wave field and the reference field B_{REF}

$$\omega_{Rabi}(y) = \sqrt{2}\,\gamma\,|B_{SW}^0 \cos^2\left(\frac{\phi}{2}\right) e^{ik_y y} - B_{REF}| \quad (3)$$

where $\phi = 35°$ is the angle with respect to (w.r.t.) the film of the NV centers used in Fig. 2 and $\gamma/2\pi = 28$ GHz/T is the (modulus of the) electron gyromagnetic ratio. Fitting the data in Fig. 2B by Eq. 3 (including a spatial decay; see the Supplementary Materials), we extract a spin-wave amplitude $m_\perp^0 = 0.033(1)M_S$ at the location of the stripline and a decay length of 1.2(1) mm, corresponding to a Gilbert damping parameter $1.2(1) \times 10^{-4}$, which is similar to the typically reported 1×10^{-4} for films of similar thickness (*25*).

By tuning the externally applied magnetic field, we sweep the NV ESR frequency through the spin-wave band and access spin waves with different wavelengths (Fig. 3A), as schematically described in Fig. 1C. In Fig. 3 (A and B), we visualize the individual spin-wave

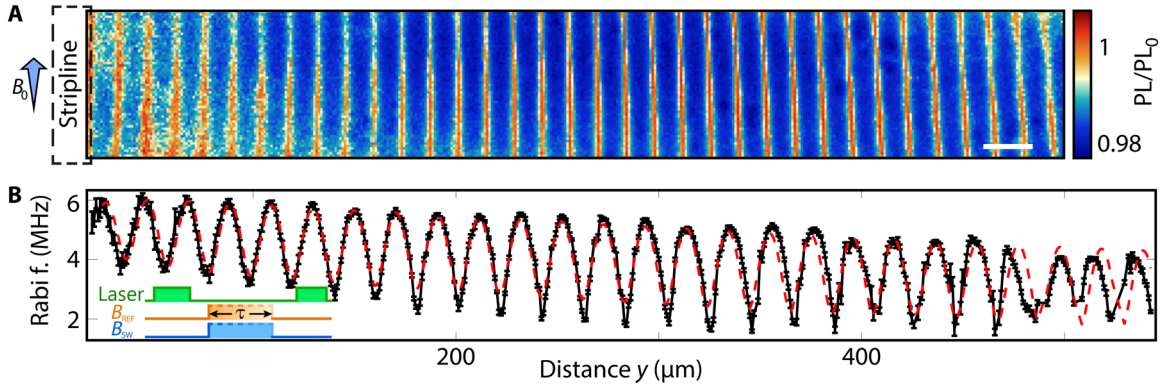

Fig. 2. Imaging coherent spin waves. (**A**) Spatial ESR contrast at $B_0 = 25$ mT when a spin wave of frequency $\omega_{SW} = \omega_- = 2\pi \times 2.17$ GHz is excited by a microwave current in the stripline (length of 2 mm, width of 30 μm, and thickness of 200 nm) at the left image edge. The NV photoluminescence with applied microwaves (PL) is normalized to that without applied microwaves (PL$_0$). The NV-YIG distance at the stripline was 1.8(2) μm, determined by measuring the field of a DC stripline current (Supplementary Materials). Scale bar, 20 μm. (**B**) Rabi frequency $\omega_{Rabi}/2\pi$ versus distance from the stripline. $\omega_{SW} = \omega_- = 2\pi \times 2.11$ GHz, $B_0 = 27$ mT. In (A) and (B), the microwaves were split between the stripline and a bonding wire, located ~100 μm above the YIG and oriented along y to generate a spatially homogeneous field B_{REF}, creating an interference pattern (see text). Red line: Fit to a model including the field of the stripline, the bonding wire, and the spin waves (section S3.3.2). Inset: Measurement sequence. Laser pulses (1 μs) are used to initialize and read out the NV spins. Microwave pulses (duration τ) drive Rabi oscillations. ω_{Rabi} was calculated from the measured $\omega_{Rabi,0}$ using $\omega_{Rabi} = \sqrt{\omega_{Rabi,0}^2 - \Delta^2}$ to account for a $\Delta = 2\pi \times 1.5$ MHz detuning between the drive frequency and the two hyperfine-split ESR resonances caused by the ^{15}N nuclear spin.

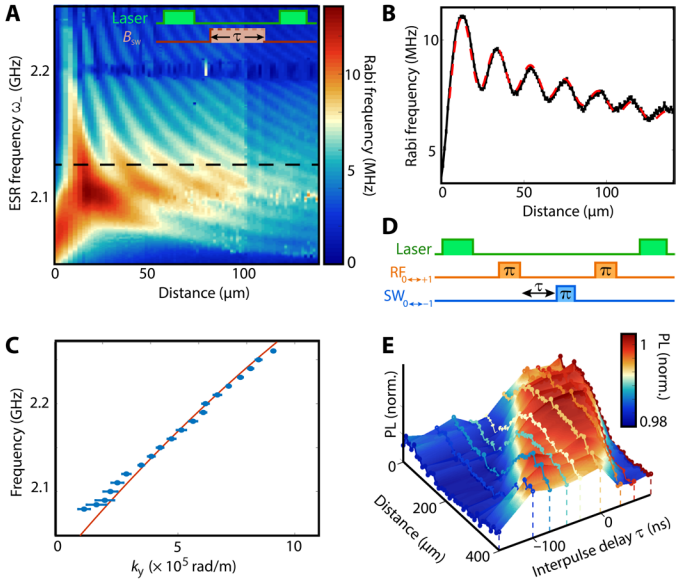

Fig. 3. Spin-wave dispersion in the space and time domains. (**A**) NV Rabi frequency versus microwave drive frequency and distance from the stripline. The feature at 2.2 GHz matches the first perpendicular spin-wave mode (Supplementary Materials). Inset: Measurement sequence. (**B**) Linecut of (A) with fit (red line) at 2.119 GHz. (**C**) Blue dots: Spin-wave frequency versus wave number extracted from (A). Red line: Calculated spin-wave dispersion. (**D**) Pulse sequence for studying spin-wave packets in the time domain [see text for details; data in (E)]: Laser pulses (1 μs) are used for NV spin initialization and readout. Two reference (RF) π pulses separated by 100 ns are applied at the $0 \leftrightarrow +1$ ESR frequency via a wire above the sample. After a time τ from the end of the first RF pulse, a spin wave–mediated π-pulse (SW) is generated at the $0 \leftrightarrow -1$ ESR frequency. (**E**) Normalized NV photoluminescence (PL) during the first 400 ns of the laser readout pulse [see (D)] versus distance from the stripline and delay time τ. Negative τ indicates a spin-wave packet generated before the first RF pulse. For example, for $\tau = -100$ ns (i.e., the spin-wave pulse is generated 100 ns before the first RF pulse), the signal rises at 360 μm, indicating a spin-wave group velocity of 3.6 km/s. Circles, data; colored surface, interpolation.

fronts using the interference between the direct stripline field and the stray field of the propagating spin wave. We extract the spin-wave dispersion from the frequency dependence of the wavelength (Fig. 3C). This dispersion matches the one calculated using values of the saturation magnetization M_s and film thickness d determined by independent measurements (Supplementary Materials).

Traveling spin-wave packets can be used for pulsed quantum control of distant spins such as those of the NV centers (*19*, *20*). Understanding the distance-dependent response of the spins to an applied control sequence requires knowledge of the spin-wave group velocity. We demonstrate a time-domain characterization of the spin-wave propagation using pulsed control of the NV spins (Fig. 3, D and E). In our measurement scheme (Fig. 3D), the NV spins at a target distance from the stripline are prepared in $m_s = 0$ using a green laser pulse. A spin-wave pulse (excited by the stripline) flips the NV spins into the dark $m_s = -1$ state only if it arrives either before or after a set of two reference pulses acting on the $0 \leftrightarrow +1$ transition (generated by a wire above the sample), resulting in low photoluminescence upon spin readout. In contrast, if the spin-wave pulse reaches the NVs between the two reference pulses, then it does not affect the NV spins because they are in $m_s = +1$ due to the first reference pulse. The second reference pulse subsequently flips the spin back to the bright $m_s = 0$ state, resulting in high photoluminescence upon spin readout. Measurements as a function of time between spin-wave and reference pulses and distance from the stripline reveal the spin-wave packet in the time domain and allow the extraction of the group velocity (Fig. 3E). We find a velocity of 3.6(2) km/s at a frequency of 2.169 GHz and a wavelength of 12 μm, consistent with the YIG spin-wave dispersion.

The 2-mm-long stripline used in Figs. 2 and 3 corresponds to an effectively one-dimensional situation. We now turn to spin waves injected by a shorter stripline with a length comparable to the scanned area (Fig. 4A). We observe a focused emission pattern that is dominated by spin-wave beams traveling at specific angles (Fig. 4, B and C). Such "caustics" occur when the dispersion is strongly

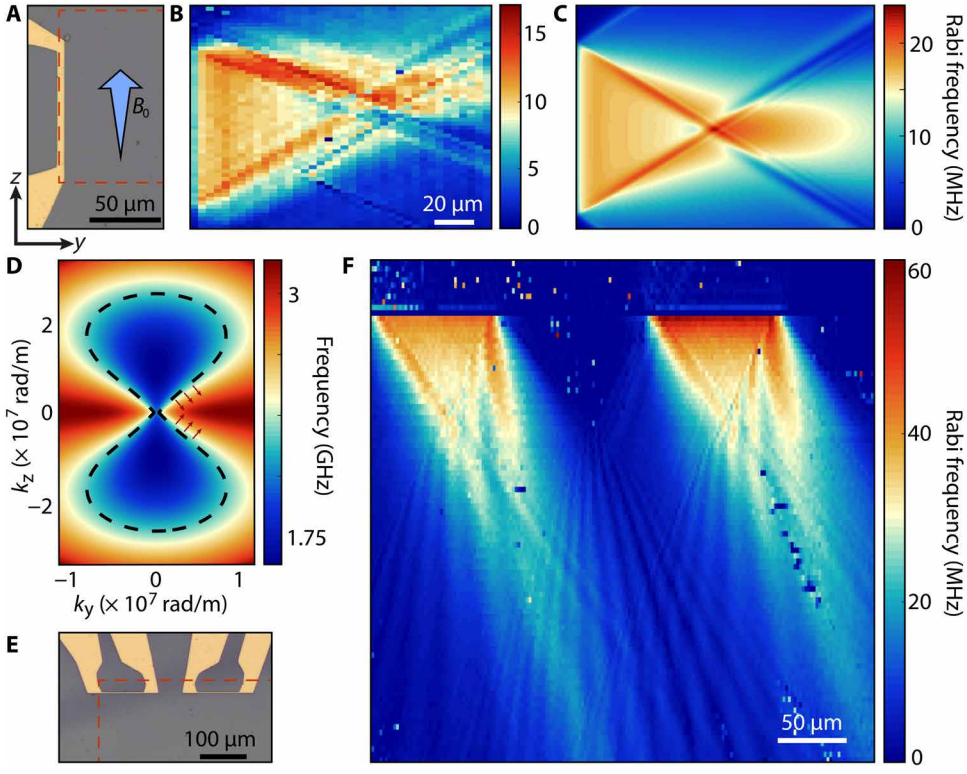

Fig. 4. Imaging interference and caustics of spin waves excited by one and two short striplines. (**A**) Optical micrograph of the stripline (width of 5 μm) used to excite spin waves. The dashed red lines indicate the region where (B) is acquired. (**B**) Rabi frequency map corresponding to the dashed region of (A) for B_0 = 27.1 mT and $\omega/2\pi$ = 2.11 GHz. The small asymmetry is attributed to a small misalignment of B_0 with respect to the striplines. (**C**) Simulation of the emission pattern observed in (B). (**D**) Calculated two-dimensional spin-wave dispersion relation $\omega(k_y, k_z)/2\pi$ at B_0 = 20.5 mT. The dashed line is an isofrequency contour at 2.292 GHz, indicating which wave vectors can be excited at this frequency and field. Red arrows indicate the direction of the spin-wave caustics. (**E**) Optical micrographs of the two injector striplines of width 2.5 μm. The dashed lines indicates the region where (F) is acquired. (**F**) Rabi frequency map under simultaneous driving of the two striplines, showing unidirectional excitation of autofocused spin-wave patterns that interfere and drive NV Rabi oscillations via their chiral magnetic stray fields.

anisotropic (*26*, *27*). They can be understood in terms of stationary points in the isofrequency curves in reciprocal space (Fig. 4D). In optics, such an isofrequency curve $k_z = k_z(k_y)$ is called "slowness" curve, because it is perpendicular to the group velocity $\boldsymbol{v}_G = \nabla_{\boldsymbol{k}}\omega(\boldsymbol{k})$. The states for which the angle of the group velocity $\theta = -\arctan(dk_z(k_y)/dk_y)$ is stationary along the curve, i.e., when $d\theta/dk_y \propto d^2k_z(k_y)/dk_y^2 = 0$, dominate emission, generating high-intensity spin-wave beams. The external magnetic field and the drive frequency can tune the beam direction and intensity (*26*, *27*), providing opportunities to optimize the efficiency of spin wave–mediated magnetic field driving of distant spins at target locations.

Last, we image the interference between spin waves excited by two adjacent striplines on the YIG chip (Fig. 4, E and F), which shows rich interference patterns radiating from the three crossing points of the main caustics (i.e., ~80 μm from the striplines edge). The strongly anisotropic spin-wave dispersion causes a triangular "dark" region between the striplines in which no spin waves are detected, because spin waves traveling at small angles with respect to the equilibrium magnetization direction or having large wave numbers are neither efficiently excited (when the wavelength is shorter than the half-width of the stripline) nor efficiently detected due to the ~1-μm NV-sample distance. The downward directionality of the observed spin-wave patterns has two causes: The chiral spin-wave field has the correct handedness to drive the ω_- NV transition, and the handedness of the stripline field excites downward-propagating spin waves more efficiently (Supplementary Materials). We note that these waves are not intrinsically directional because their wavelength far exceeds the film thickness (*28*), in contrast with Damon-Eshbach surface waves in thick films (*29*). The observed directionality and interference patterns agree well with linear response calculations of the nonlocal dynamic susceptibility and the spatial profile of the microwave drive field, as described in the Supplementary Materials. These quantitative measurements of the spin wave–generated rotating magnetic stray fields illustrate the power of NV-based magnetic resonance imaging in magnonics.

DISCUSSION

Our results demonstrate that ensembles of NV spins in diamonds enable quantitative, phase-sensitive magnetic imaging of coherent spin waves in thin-film magnets. A theoretical analysis explains the NV sensor signals in terms of the rotating stray fields generated by spin waves that are excited unidirectionally by the stripline magnetic field. In contrast to other spin-wave imaging techniques, our technique images spin waves by their microwave magnetic stray fields. This does not require a specific spin-photon or spin-electron interaction and enables imaging spin waves through optically opaque materials. These capabilities provide new opportunities, e.g., for

studying top-gated materials and the interaction of spin waves with magnetic and nonmagnetic materials placed on top of a magnetic film, which play an important role for spin-wave excitation and damping and form the basis for nonreciprocal devices (*30*). NV magnetometry also allows high-resolution imaging of electric currents (*31*), enabling spatial studies of the interaction between spin waves and charge transport.

Both the NV-sample distance and the optical resolution of our microscope limit the resolution of our technique. The typical NV-magnet distances are here 0.5 to 2 μm (limited by, e.g., dust particles), comparable to our diffraction-limited optical resolution. Shallow NV centers in diamond chips that are wafer-bonded to (i.e., in direct contact with) a magnetic sample should allow the detection of spin waves with wavelengths comparable to the implantation depth of the NV centers of a few nanometers (*32*)— albeit without phase sensitivity. This requires resonance between the spin waves and the NV sensors, e.g., by tuning a magnetic field and/or magnetic anisotropies. This may be difficult for magnetically hard materials. We can probe nonresonant spin waves by detecting the Stark shift that they impart on the sensor spins (*33*) or by detecting intraband spin-wave transitions using NV spin relaxometry (*34*). Phase-sensitive imaging of spin waves with wavelengths below the diffraction limit could be enabled using specialized NV control sequences such as phase encoding schemes (*35*). Furthermore, the techniques presented here are directly transferrable to single-NV scanning probe microscopes with real-space resolution on the 10-nm scale (*36*).

Our results pave the way for studying spin waves in other magnetic material systems such as magnetic nanodevices and atomically thin magnets. NV magnetometry works at cryogenic temperatures (*37*–*39*), allowing studies of magnets with low Curie temperatures such as complex oxide or van der Waals magnets. Because the dipole density per unit area $M_s d = 3.6\times 10^3\ \mu_B/\mathrm{nm}^2$ of the YIG film studied here is only about two orders of magnitude above the $16\ \mu_B/\mathrm{nm}^2$ of the monolayer van der Waals magnet CrI_3 (*22*), the magnetic stray fields generated by spin waves in such monolayer magnets are within the sensitivity range of NV-based magnetic imaging. The sensitivity of our technique is rooted in measuring the sum of a reference field and the spin-wave field. A good strategy for measuring weak spin-wave fields is to apply a strong reference field and measure the variations in the Rabi frequency caused by the spin-wave field, because Rabi frequency variations of ~100 kHz can easily be detected (the average error bar in Fig. 2B is 75 kHz). We can further increase the sensitivity by applying a stronger reference field, which decouples the NV spin from noise sources (*40*). Increasing the microwave drive current and reducing the NV-sample distance [for instance, by depositing a van der Waals material directly onto the diamond (*41*)] would further increase the detection capability.

MATERIALS AND METHODS

Sample fabrication

The diamond samples used in this work are chemical vapor deposition (CVD)–grown, electronic-grade type IIa diamonds (Element 6), laser-cut, and polished down to 2 mm × 2 mm × 0.05 mm chips (Almax easyLab). These chips were cleaned with nitric acid, and the top ~5 μm were removed using inductively-coupled plasma (ICP) reactive ion etching (30 min Ar/Cl, 20 min O_2) to mitigate polishing damage. The chips were subsequently implanted with ^{15}N ions at 6 keV with a dose of 1×10^{13} ions/cm^2 (INNOViON), tri-acid cleaned (mixture of nitric, sulfuric, and perchloric acid, 1:1:1), annealed at 800°C for 4 hours at 10^{-6} mbar, and tri-acid cleaned again to remove possibly graphitized layers on the surface, resulting in an estimated density of NV centers of ~1×10^{11} NV/cm^2 at a depth of ~10 to 20 nm.

The YIG films were 245 nm thick, grown on gadolinium gallium garnet (GGG) substrates by liquid-phase epitaxy (Matesy GmbH). Before stripline fabrication, the YIG/GGG chips were sonicated in acetone and cleaned for a few seconds in an O_2 descum plasma to remove contaminants. Striplines for spin-wave excitation were fabricated directly onto the YIG films by e-beam lithography using a PMMA(A8 495)/PMMA(A3 950) double-layer resist and subsequent e-beam evaporation of Cr/Au (5 nm/200 nm). To attach an NV-containing diamond to the YIG film, a small droplet of isopropanol was deposited onto the YIG, on top of which a diamond chip was placed, with the NV surface facing down. The diamond chip was gently pressed down until the isopropyl alcohol had evaporated (*42*). The resulting NV-YIG distance was measured to be 1.8(2) μm (see fig. S1).

Measurement setup

The optical setup used for all the measurements was a homebuilt confocal microscope. A 515-nm laser (Cobolt 06-MLD) was used for optical excitation of the NV centers, focused to a diffraction-limited spot by an Olympus 50×, numerical aperture = 0.95 objective. The NV luminescence was collected by the same objective, separated from the excitation light by a Semrock dichroic mirror and long-pass filter (617-nm cutoff), spatially filtered by a pinhole, and detected using a single-photon counting module (Laser Components). The microwaves signals used for driving NVs and spin waves were generated using Rohde & Schwarz microwave generators (SGS100A). The reference field B_{REF} used to produce the interference pattern in Fig. 2 was generated by a wire located ~200 μm above the diamond and oriented perpendicularly to the stripline. To simultaneously drive the pair of striplines in Fig. 4, the microwave excitation was split using a Mini-Circuits power combiner (ZFRSC-123-S+). A National Instruments data acquisition card was used for triggering the data acquisition, while a SpinCore programmable pulse generator (PulseBlaster ESR-PRO 500) was used to control the timing sequences of the laser excitation, microwaves, and detection window. The photons were collected during the first 300 to 400 ns of the laser readout pulse, which was kept fixed to 1 μs. All measurements were performed at room temperature.

NV magnetometry

The NV spins are initialized and read out using nonresonant optical excitation at 515 nm. To measure NV spin rotations (Rabi oscillations), we first apply a ~1-μs green laser pulse to polarize the NV spin into the $m_s = 0$ state. A subsequently applied microwave magnetic field resonant with an NV ESR frequency drives Rabi oscillations between the corresponding NV spin states ($m_s = 0$ and -1 in Fig. 2B). The NV spin state is read out by applying a laser pulse and measuring the spin-dependent photoluminescence that results from spin-selective nonradiative decay via a metastable singlet state. The ESR frequencies of the four NV families (Fig. 1D) in a magnetic field B_0 are determined by the NV spin Hamiltonian $H = DS_z^2 + \gamma \mathbf{B}_0 \cdot \mathbf{S}$, where γ is the electron gyromagnetic ratio, D is the zero-field splitting (2.87 GHz), and $S_{(i=x,y,z)}$ is the Pauli spin matrices for a spin 1. We apply the magnetic field B_0 using a small permanent magnet (diameter, 1 cm; height, 2 cm).

Wavelength of the spin waves driving NV Rabi oscillations

We excite spin waves at a frequency that matches the ω_- ESR transition of the NV spins, allowing us to detect the spin waves via the resulting NV Rabi oscillations. Hence, for a given field B_0 applied along the NV axis, the wave number of the spin waves driving Rabi oscillations is determined by equating the NV frequency $\omega_-/2\pi = D - \gamma B_0$ to the spin-wave frequency given by the spin-wave dispersion (eq. S10)

$$\frac{\omega(B_0,k)}{\gamma\mu_0 M_s \hbar} = \sqrt{\left(\frac{B_0\cos\theta}{\mu_0 M_s} + \alpha_{ex}k^2 + \frac{1-e^{-|k_y|d}}{|k_y|d}\right)\left(\frac{B_0\cos\theta}{\mu_0 M_s} + \alpha_{ex}k^2 + \frac{k_y^2}{k^2}\left(1 - \frac{1-e^{-|k_y|d}}{|k_y|d}\right)\right)}$$

where k is the SW wave number; k_y is its in-plane component perpendicular to the static magnetization; μ_0 is the magnetic permeability of vacuum; and M_s, $\alpha_{ex} = 3.0 \times 10^{-16}$ m^2, and d are the YIG saturation magnetization, exchange constant (*23*), and thickness, respectively.

SUPPLEMENTARY MATERIALS

Supplementary material for this article is available at http://advances.sciencemag.org/cgi/content/full/6/46/eabd3556/DC1

REFERENCES AND NOTES

1. V. V. Kruglyak, S. O. Demokritov, D. Grundler, Magnonics. *J. Phys. D Appl. Phys.* **43**, 264001 (2010).
2. A. V. Chumak, V. I. Vasyuchka, A. A. Serga, B. Hillebrands, Magnon spintronics. *Nat. Phys.* **11**, 453–461 (2015).
3. K. Vogt, F. Y. Fradin, J. E. Pearson, T. Sebastian, S. D. Bader, B. Hillebrands, A. Hoffmann, H. Schultheiss, Realization of a spin-wave multiplexer. *Nat. Commun.* **5**, 3727 (2014).
4. A. V. Chumak, A. A. Serga, B. Hillebrands, Magnon transistor for all-magnon data processing. *Nat. Commun.* **5**, 4700 (2014).
5. L. J. Cornelissen, J. Liu, B. J. van Wees, R. A. Duine, Spin-current-controlled modulation of the magnon spin conductance in a three-terminal magnon transistor. *Phys. Rev. Lett.* **120**, 097702 (2018).
6. V. E. Demidov, H. Ulrichs, S. V. Gurevich, S. O. Demokritov, V. S. Tiberkevich, A. N. Slavin, A. Zholud, S. Urazhdin, Synchronization of spin Hall nano-oscillators to external microwave signals. *Nat. Commun.* **5**, 3179 (2014).
7. Q. Wang, P. Pirro, R. Verba, A. Slavin, B. Hillebrands, A. V. Chumak, Reconfigurable nanoscale spin-wave directional coupler. *Sci. Adv.* **4**, e1701517 (2018).
8. T. Warwick, K. Franck, J. B. Kortright, G. Meigs, M. Moronne, S. Myneni, E. Rotenberg, S. Seal, W. F. Steele, H. Ade, A. Garcia, S. Cerasari, J. Denlinger, S. Hayakawa, A. P. Hitchcock, T. Tyliszczak, J. Kikuma, E. G. Rightor, H.-J. Shin, B. P. Tonner, A scanning transmission x-ray microscope for materials science spectromicroscopy at the advanced light source. *Rev. Sci. Instrum.* **69**, 2964–2973 (1998).
9. V. Sluka, T. Schneider, R. A. Gallardo, A. Kákay, M. Weigand, T. Warnatz, R. Mattheis, A. Roldán-Molina, P. Landeros, V. Tiberkevich, A. Slavin, G. Schütz, A. Erbe, A. Deac, J. Lindner, J. Raabe, J. Fassbender, S. Wintz, Emission and propagation of 1D and 2D spin waves with nanoscale wavelengths in anisotropic spin textures. *Nat. Nanotechnol.* **14**, 328–333 (2019).
10. T. Sebastian, K. Schultheiss, B. Obry, B. Hillebrands, H. Schultheiss, Micro-focused Brillouin light scattering: Imaging spin waves at the nanoscale. *Front. Phys.* **3**, 35 (2015).
11. Y. Acremann, C. H. Back, M. Buess, O. Portmann, A. Vaterlaus, D. Pescia, H. Melchior, Imaging precessional motion of the magnetization vector. *Science* **290**, 492–495 (2000).
12. L. Rondin, J.-P. Tetienne, T. Hingant, J.-F. Roch, P. Maletinsky, V. Jacques, Magnetometry with nitrogen-vacancy defects in diamond. *Rep. Prog. Phys.* **77**, 056503 (2014).
13. F. Casola, T. van der Sar, A. Yacoby, Probing condensed matter physics with magnetometry based on nitrogen-vacancy centres in diamond. *Nat. Rev. Mater.* **3**, 17088 (2018).
14. I. Gross, W. Akhtar, V. Garcia, L. J. Martínez, S. Chouaieb, K. Garcia, C. Carrétéro, A. Barthélémy, P. Appel, P. Maletinsky, J.-V. Kim, J. Y. Chauleau, N. Jaouen, M. Viret, M. Bibes, S. Fusil, V. Jacques, Real-space imaging of non-collinear antiferromagnetic order with a single-spin magnetometer. *Nature* **549**, 252–256 (2017).
15. L. Rondin, J.-P. Tetienne, S. Rohart, A. Thiaville, T. Hingant, P. Spinicelli, J.-F. Roch, V. Jacques, Stray-field imaging of magnetic vortices with a single diamond spin. *Nat. Commun.* **4**, 2279 (2013).
16. Y. Dovzhenko, F. Casola, S. Schlotter, T. X. Zhou, F. Büttner, R. L. Walsworth, G. S. D. Beach, A. Yacoby, Magnetostatic twists in room-temperature skyrmions explored by nitrogen-vacancy center spin texture reconstruction. *Nat. Commun.* **9**, 2712 (2018).
17. T. van der Sar, F. Casola, R. Walsworth, A. Yacoby, Nanometre-scale probing of spin waves using single-electron spins. *Nat. Commun.* **6**, 7886 (2015).
18. C. Du, T. van der Sar, T. X. Zhou, P. Upadhyaya, F. Casola, H. Zhang, M. C. Onbasli, C. A. Ross, R. L. Walsworth, Y. Tserkovnyak, A. Yacoby, Control and local measurement of the spin chemical potential in a magnetic insulator. *Science* **357**, 195–198 (2017).
19. P. Andrich, C. F. de las Casas, X. Liu, H. L. Bretscher, J. R. Berman, F. J. Heremans, P. F. Nealey, D. D. Awschalom, Long-range spin wave mediated control of defect qubits in nanodiamonds. *npj Quantum Inf.* **3**, 28 (2017).
20. D. Kikuchi, D. Prananto, K. Hayashi, A. Laraoui, N. Mizuochi, M. Hatano, E. Saitoh, Y. Kim, C. A. Meriles, T. An, Long-distance excitation of nitrogen-vacancy centers in diamond via surface spin waves. *Appl. Phys. Express* **10**, 103004 (2017).
21. C. S. Wolfe, V. P. Bhallamudi, H. L. Wang, C. H. Du, S. Manuilov, R. M. Teeling-Smith, A. J. Berger, R. Adur, F. Y. Yang, P. C. Hammel, Off-resonant manipulation of spins in diamond via precessing magnetization of a proximal ferromagnet. *Phys. Rev. B* **89**, 180406 (2014).
22. L. Thiel, Z. Wang, M. A. Tschudin, D. Rohner, I. Gutiérrez-Lezama, N. Ubrig, M. Gibertini, E. Giannini, A. F. Morpurgo, P. Maletinsky, Probing magnetism in 2D materials at the nanoscale with single-spin microscopy. *Science* **364**, 973–976 (2019).
23. A. A. Serga, A. V. Chumak, B. Hillebrands, YIG magnonics. *J. Phys. D Appl. Phys.* **43**, 264002 (2010).
24. T. Yu, Y. M. Blanter, G. E. W. Bauer, Chiral pumping of spin waves. *Phys. Rev. Lett.* **123**, 247202 (2019).
25. C. Dubs, O. Surzhenko, R. Linke, A. Danilewsky, U. Brückner, J. Dellith, Sub-micrometer yttrium iron garnet LPE films with low ferromagnetic resonance losses. *J. Phys. D Appl. Phys.* **50**, 204005 (2017).
26. T. Schneider, A. A. Serga, A. V. Chumak, C. W. Sandweg, S. Trudel, S. Wolff, M. P. Kostylev, V. S. Tiberkevich, A. N. Slavin, B. Hillebrands, Nondiffractive subwavelength wave beams in a medium with externally controlled anisotropy. *Phys. Rev. Lett.* **104**, 197203 (2010).
27. R. Gieniusz, H. Ulrichs, V. D. Bessonov, U. Guzowska, A. I. Stognii, A. Maziewski, Single antidot as a passive way to create caustic spin-wave beams in yttrium iron garnet films. *Appl. Phys. Lett.* **102**, 102409 (2013).
28. M. Mohseni, R. Verba, T. Brächer, Q. Wang, D. A. Bozhko, B. Hillebrands, P. Pirro, Backscattering immunity of dipole-exchange magnetostatic surface spin waves. *Phys. Rev. Lett.* **122**, 197201 (2019).
29. J. R. Eshbach, R. W. Damon, Surface magnetostatic modes and surface spin waves. *Phys. Rev.* **118**, 1208–1210 (1960).
30. J. Chen, T. Yu, C. Liu, T. Liu, M. Madami, K. Shen, J. Zhang, S. Tu, M. S. Alam, K. Xia, M. Wu, G. Gubbiotti, Y. M. Blanter, G. E. W. Bauer, H. Yu, Excitation of unidirectional exchange spin waves by a nanoscale magnetic grating. *Phys. Rev. B.* **100**, 104427 (2019).
31. J.-P. Tetienne, N. Dontschuk, D. A. Broadway, A. Stacey, D. A. Simpson, L. C. L. Hollenberg, Quantum imaging of current flow in graphene. *Sci. Adv.* **3**, e1602429 (2017).
32. T. Rosskopf, A. Dussaux, K. Ohashi, M. Loretz, R. Schirhagl, H. Watanabe, S. Shikata, K. M. Itoh, C. L. Degen, Investigation of surface magnetic noise by shallow spins in diamond. *Phys. Rev. Lett.* **112**, 147602 (2014).
33. C. Wei, A. S. M. Windsor, N. B. Manson, A strongly driven two-level atom revisited: Bloch-Siegert shift versus dynamic Stark splitting. *J. Phys. B At. Mol. Opt. Phys.* **30**, 21 (1997).
34. B. Flebus, Y. Tserkovnyak, Quantum-impurity relaxometry of magnetization dynamics. *Phys. Rev. Lett.* **121**, 187204 (2018).
35. K. Arai, C. Belthangady, H. Zhang, N. Bar-Gill, S. J. Devience, P. Cappellaro, A. Yada, R. L. Walsworth, Fourier magnetic imaging with nanoscale resolution and compressed sensing speed-up using electronic spins in diamond. *Nat. Nanotechnol.* **10**, 859–864 (2015).
36. G. Balasubramanian, I. Y. Chan, R. Kolesov, M. Al-Hmoud, J. Tisler, C. Shin, C. Kim, A. Wojcik, P. R. Hemmer, A. Krueger, T. Hanke, A. Leitenstorfer, R. Bratschitsch, F. Jelezko, J. Wrachtrup, Nanoscale imaging magnetometry with diamond spins under ambient conditions. *Nature* **455**, 648–651 (2008).
37. L. Thiel, D. Rohner, M. Ganzhorn, P. Appel, E. Neu, B. Müller, R. Kleiner, D. Koelle, P. Maletinsky, Quantitative nanoscale vortex imaging using a cryogenic quantum magnetometer. *Nat. Nanotechnol.* **11**, 677–681 (2016).
38. M. Pelliccione, A. Jenkins, P. Ovartchaiyapong, C. Reetz, E. Emmanouilidou, N. Ni, A. C. Bleszynski Jayich, Scanned probe imaging of nanoscale magnetism at cryogenic temperatures with a single-spin quantum sensor. *Nat. Nanotechnol.* **11**, 700–705 (2016).

39. E. Schaefer-Nolte, F. Reinhard, M. Ternes, J. Wrachtrup, K. Kern, A diamond-based scanning probe spin sensor operating at low temperature in ultra-high vacuum. *Rev. Sci. Instrum.* **85**, 013701 (2014).
40. J.-M. Cai, B. Naydenov, R. Pfeiffer, L. P. McGuinness, K. D. Jahnke, F. Jelezko, M. B. Plenio, A. Retzker, Robust dynamical decoupling with concatenated continuous driving. *New J. Phys.* **14**, 113023 (2012).
41. S. E. Lillie, N. Dontschuk, D. A. Broadway, D. L. Creedon, L. C. L. Hollenberg, J.-P. Tetienne, Imaging graphene field-effect transistors on diamond using nitrogen-vacancy microscopy. *Phys. Rev. Appl.* **12**, 024018 (2019).
42. S. Bogdanović, M. S. Z. Liddy, S. B. Van Dam, L. C. Coenen, T. Fink, M. Lončar, R. Hanson, Robust nano-fabrication of an integrated platform for spin control in a tunable microcavity. *APL Photonics* **2**, 126101 (2017).
43. M. A. W. Schoen, J. M. Shaw, H. T. Nembach, M. Weiler, T. J. Silva, Radiative damping in waveguide-based ferromagnetic resonance measured via analysis of perpendicular standing spin waves in sputtered permalloy films. *Phys. Rev. B* **92**, 184417 (2015).
44. B. A. Kalinikos, A. N. Slavin, Theory of dipole-exchange spin wave spectrum for ferromagnetic films with mixed exchange boundary conditions. *J. Phys. C Solid State Phys.* **19**, 7013–7033 (1986).
45. J. D. Jackson, *Classical Electrodynamics* (Wiley, 1998).
46. L. Novotny, B. Hecht, *Principles of Nano-optics* (Cambridge Univ. Press, 2006).
47. T. Yu, C. Liu, H. Yu, Y. M. Blanter, G. E. W. Bauer, Chiral excitation of spin waves in ferromagnetic films by magnetic nanowire gratings. *Phys. Rev. B* **99**, 134424 (2019).

Acknowledgments

Funding: This work was supported by the Dutch Research Council (NWO) as part of the Frontiers of Nanoscience (NanoFront) program through NWO Projectruimte grant 680.91.115, JSPS KAKENHI grant no. 19H006450, and Kavli Institute of Nanoscience Delft.

Author contributions: I.B., J.J.C., and T.v.d.S. designed the experiment. I.B. fabricated the diamond-YIG samples, realized the imaging setup, performed the NV measurements, and analyzed the data. B.G.S. prepared the diamonds. C.C.P. performed the vector network analyzer (VNA) measurements, for which J.J.C. fabricated the samples. T.Y., Y.M.B., and G.E.W.B. developed the theoretical model describing spin-wave caustics and interference. I.B. and T.v.d.S. wrote the manuscript with help from all coauthors. J.A. contributed to the discussions of the results and the manuscript. **Competing interests:** The authors declare that they have no competing interests. **Data and materials availability:** All data contained in the figures are available at Zenodo.org with the identifier 10.5281/zenodo.4005488. Additional data related to this paper may be requested from the authors.

Submitted 16 June 2020
Accepted 25 September 2020
Published 11 November 2020
10.1126/sciadv.abd3556

Citation: I. Bertelli, J. J. Carmiggelt, T. Yu, B. G. Simon, C. C. Pothoven, G. E. W. Bauer, Y. M. Blanter, J. Aarts, T. van der Sar, Magnetic resonance imaging of spin-wave transport and interference in a magnetic insulator. *Sci. Adv.* **6**, eabd3556 (2020).

Science Advances

Magnetic resonance imaging of spin-wave transport and interference in a magnetic insulator

Iacopo Bertelli, Joris J. Carmiggelt, Tao Yu, Brecht G. Simon, Coosje C. Pothoven, Gerrit E. W. Bauer, Yaroslav M. Blanter, Jan Aarts and Toeno van der Sar

Sci Adv **6** (46), eabd3556.
DOI: 10.1126/sciadv.abd3556